Astronomy & Astrophysics

L ETTER TO THE E DITOR

Characterization and formation of on-disk spicules in the Ca II K and Mg II k spectral lines

Souvik Bose[1,2], Vasco M. J. Henriques[1,2], Jayant Joshi[1,2], and Luc Rouppe van der Voort[1,2]

[1] Institute of Theoretical Astrophysics, University of Oslo, PO Box 1029, Blindern 0315 Oslo, Norway
e-mail: souvik.bose@astro.uio.no
[2] Rosseland Centre for Solar Physics, University of Oslo, PO Box 1029, Blindern 0315, Oslo, Norway

ABSTRACT

We characterize, for the first time, type-II spicules in Ca II K 3934 Å using the CHROMIS instrument at the Swedish 1 m Solar Telescope. We find that their line formation is dominated by opacity shifts with the K_3 minimum best representing the velocity of the spicules. The K_2 features are either suppressed by the Doppler-shifted K_3 or enhanced via increased contribution from the lower layers, leading to strongly enhanced but unshifted K_2 peaks, with widening towards the line core as consistent with upper-layer opacity removal via Doppler-shift. We identify spicule spectra in concurrent IRIS Mg II k 2796 Å observations with very similar properties. Using our interpretation of spicule chromospheric line formation, we produce synthetic profiles that match observations.

Key words. Sun: chromosphere – line: profiles – line: formation – radiative transfer – opacity

1. Introduction

Spicules are ubiquitous and highly dynamic features that permeate the solar chromosphere. They can be divided into two categories, the second of which (type-II spicules) are more dynamic with shorter lifetimes, vigorous sideways motion, and high apparent velocities (De Pontieu et al. 2007; Tsiropoula et al. 2012; Pereira et al. 2012, 2016). Type-II spicules can be heated beyond chromospheric temperatures and during their lifetime become visible in the transition region (De Pontieu et al. 2011; Pereira et al. 2014; Rouppe van der Voort et al. 2015) and coronal diagnostics (De Pontieu et al. 2011, 2017a; Henriques et al. 2016; Kuridze et al. 2016). These characteristics form the basis for attributing type-II spicules an important role in mass loading and heating of the solar corona (see, e.g., Martínez-Sykora et al. 2017; Tian 2017; Kontogiannis et al. 2018; Martínez-Sykora et al. 2018) with potentially higher impact at lower temperatures (Iijima & Yokoyama 2015).

Type-II spicules have been observed as rapid Doppler excursions of the chromospheric Hα and Ca II 8542 Å spectral lines, a characteristic which led to them being called rapid blue-shifted and red-shifted excursions (RBEs and RREs, Langangen et al. 2008; Rouppe van der Voort et al. 2009; Sekse et al. 2012, 2013; Kuridze et al. 2015). Their spectral signatures have also been identified in Mg II H and K profiles (Rouppe van der Voort et al. 2015).

With the advent of the CHROMospheric Imaging Spectrometer (CHROMIS) at the Swedish 1 m Solar Telescope (SST, Scharmer et al. 2003a), it is now possible to achieve imaging spectroscopy at an unprecedented spatial resolution of better than 0″.1 at wavelengths shortward of 4000 Å. Through high-spectral-resolution imaging in the Ca II K 3934 Å line, CHROMIS unlocks the potential to uncover spicule properties at ever smaller spatial and temporal scales.

The Ca II K spectral line features similar formation properties as Mg II k showing wide damping wings and self reversals in the respective line cores. The Ca II K line is formed lower in the atmosphere than its Mg counterpart, mostly due to roughly 18 times lower abundance of calcium compared with magnesium (for recent studies of Mg II and Ca II spectral line formation, see Leenaarts et al. 2013; Bjørgen et al. 2018).

In this Letter, we use coordinated on-disk observations from the SST and Interface Region Imaging Spectrograph (IRIS, De Pontieu et al. 2014). Type-II spicules are characterized in Ca II K for the first time with the help of an unsupervised machine-learning algorithm that provides a robust characterization of millions of profiles through representative bins, with only a handful being spicules. We exploit the co-temporal and co-spatial datasets from IRIS to identify corresponding Mg II k spicule spectra. We further our understanding of spicules and spicule line-profile formation through a simple numerical experiment.

2. Observations and methods

We observed an enhanced network region close to disk center on 25 May 2017 for 97 min. From the SST, we analyzed imaging spectroscopy data in Hα acquired with the CRisp Imaging SpectroPolarimeter (CRISP, Scharmer et al. 2008) and Ca II K with CHROMIS. From IRIS, we analyzed concurrent Mg II k spectra from a 2″.32×69″.2 raster and 2796 Å Slit-Jaw Images (SJIs). The IRIS and CRISP datasets were co-aligned, and blown up to the CHROMIS pixel scale (0″.037) by cross-correlating Ca II K inner line wing with SJI 2796 Å, and the photospheric wideband channels associated with the Ca II K and Hα data, respectively. For more details of the observations and data processing, we refer to Appendix A.
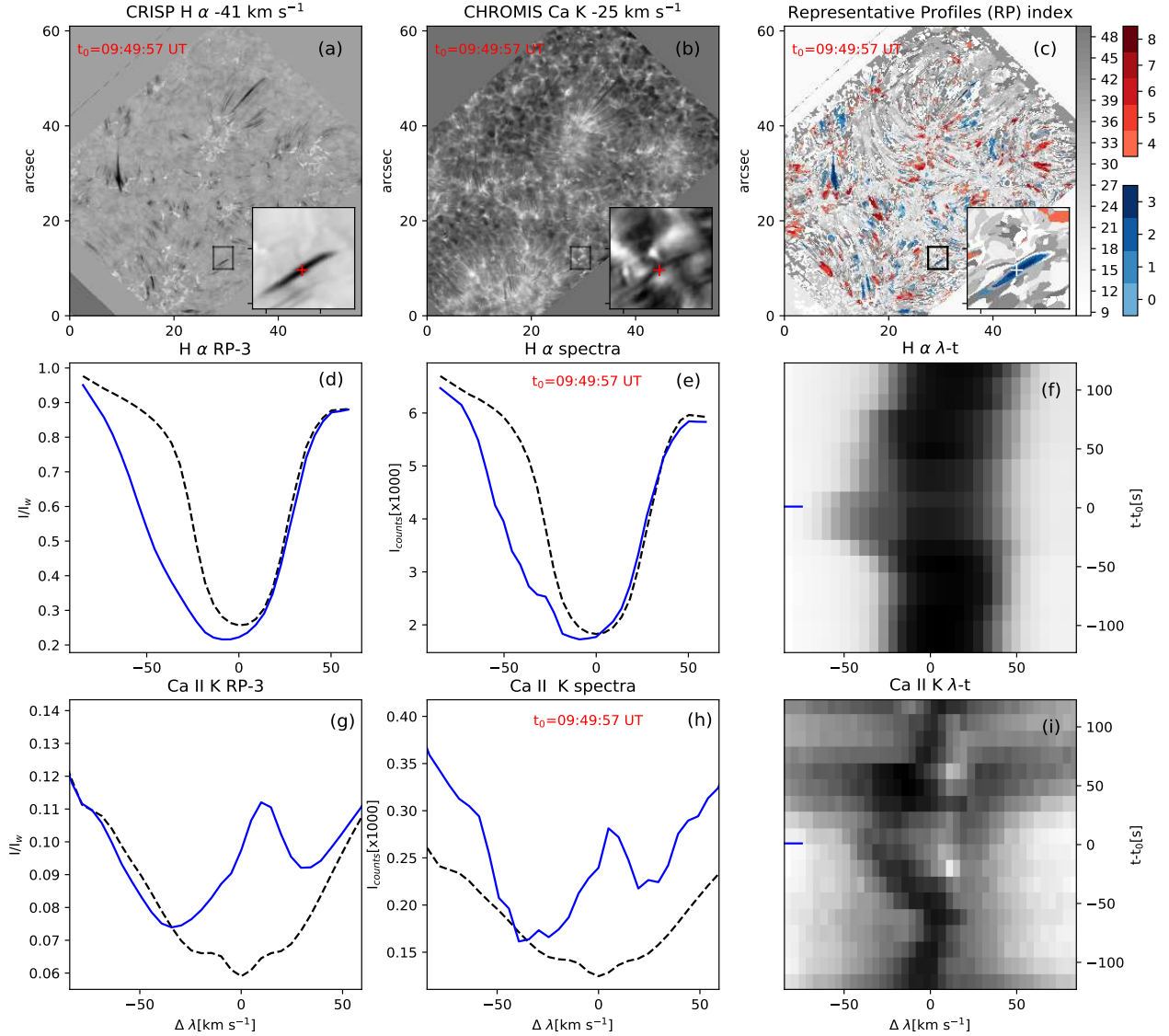
Fig. 1. Identification of RBEs in Hα and Ca II K. *Top row*: blue wing Hα (*a*) and Ca II K (*b*) spectroheliograms, and the same region color-coded in terms of RP indexing (*c*). Small insets zoom in on a selected RBE with a cross symbol marking the location for the profiles shown in blue in (*e*) and (*h*), and the spectral evolution λt-slices (*f*) and (*i*). The corresponding RP profiles are shown in (*d*) and (*g*). The blue marker in (*f*) and (*i*) indicates the time $t_0 = 09{:}49{:}57$ UTC. Reference quiet Sun profiles (RP−43) are shown as dashed lines.

Identifying rapid excursions in Ca II K is not straightforward as they have neither a sharp image contrast as in Hα (see Fig. 1a and b), nor a simple absorption profile. Therefore, we use the robust *k-means clustering* technique to identify RBEs and RREs in both these spectral regions simultaneously, based on their profiles as described in Appendix B.

3. Results and discussion

3.1. Spectral characteristics of RBEs from observations and k-means

Rapid blue-shifted excursions and RREs have most commonly been identified in Hα, and their spectra show strong absorption asymmetries in the blue or red wing. However, their Ca II K spectra show different behavior. Therefore, we apply the classical *k*-means clustering to extract their spectral characteristics. The *k*-means algorithm assigned each pixel on the common CRISP and CHROMIS field-of-view (FOV) to one representative

profile (RP), with indices 0−49. The RP indices map corresponding to one scan is shown in Fig. 1c. For better visibility, we indicate RBE-like (RRE-like) RPs in shades of blue (red) and the rest of the background in grayscale. We find that RP−0 to RP−3 show absorption in the blue wing of Hα (see Fig. 2) as characteristic to RBEs, and that RP−4 to RP−8 show the red-wing absorption typical of RREs (see Fig. 3). Darker shades of blue and red in Fig. 1c imply stronger absorption in Hα wings. Consequently, RP−1 is stronger than RP−0 and so on.

The insets in the first row of Fig. 1 zoom in on a dark thread-like feature that was identified as an RBE. It is evident that RBEs in blue wing Ca II K have reduced contrast with respect to the background compared with Hα, thereby making it difficult to identify them from spectroheliograms. However, their appearance is spatially coherent in both diagnostics. The blue-colored streak in the RP map inset (Fig. 1c) shows a clear structural resemblance to the Hα RBE, thereby strengthening our confidence in the detection from the *k*-means technique. The observed spectra and RP corresponding to the pixel indicated
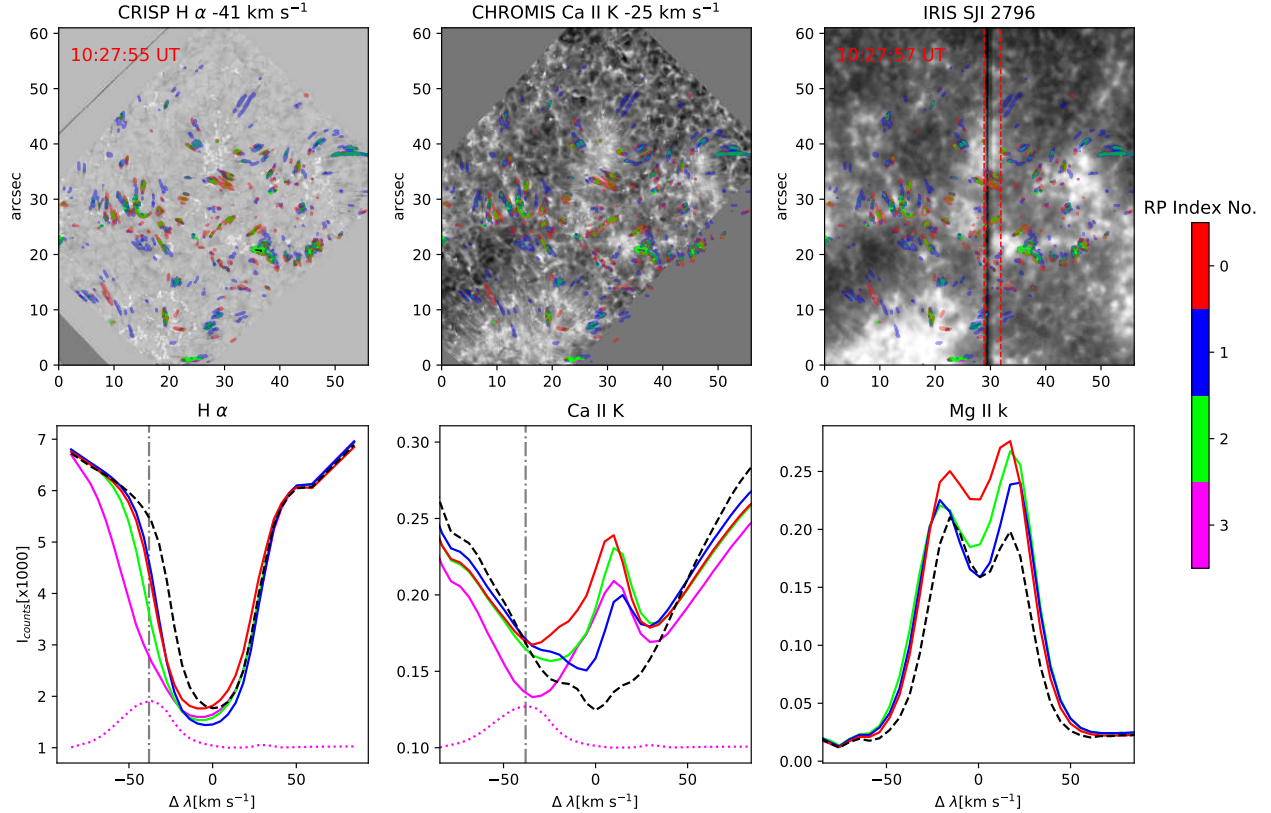
Fig. 2. Rapid blue-shifted excursions in Hα, Ca II K, and Mg II k. *Top*: spectroheliograms and slit-jaw as labeled with overplotted color-coded RP bins. *Bottom*: spectra for the RPs following the same color code. The dotted pink profile is the difference between the average Hα profile (dashed) and that of RP−3 in arbitrary units. The vertical dashed-dotted line highlights the proximity of the latter with the minimum of the Ca II K₃ RP−3 at $-38.6\,\mathrm{km\,s^{-1}}$. The dashed red lines in the SJI indicate the extent of the IRIS rasters.

with the red cross symbol are shown in the second and third rows of Fig. 1. The profile of interest belongs to RP−3 and is plotted in Fig. 1d for Hα. This profile displays significant asymmetry in the blue wing as compared to the reference quiet Sun (RP−43, dashed line), confirmed by the observed Hα spectrum shown in panel e. The temporal evolution of the spectra is shown in the wavelength-time (λt-slice; Fig. 1f) confirming the RBE "rapidity" by clearly showing its short lifetime (of ~50 s in this case) and the characteristic blue-ward asymmetry. We also show the RP, observed spectra, and λt-slice for the corresponding Ca II K RBE in the bottom row of Fig. 1. More than 90% of the events detected using k-means have a lifetime <100 s. The detailed statistical analysis will be presented in a forthcoming article. Both the representative and observed profiles have higher specific intensity compared to the quiet Sun and are significantly asymmetric with an enhanced K_{2R} peak (we follow the classic nomenclature for the K_1 to K_3 spectral features in the Ca II K line; see, for example, Fig. 1 in Rutten & Uitenbroek 1991).

The Ca II K λt-slice shows a clearer progression of the rapid blue-ward excursion, due to the higher cadence and narrower line-minimum compared with Hα, and reveals continuity between the line-minimum at rest and the line-minimum at maximum shift. Therefore, the line-minimums for the most strongly shifted spicules are likely the usual K_3 line features, merely Doppler shifted. The presented RPs in Fig. 1 are normalized as used for the k-means (see Appendix B) while the observed spectral pair of Hα and Ca II K have been plotted in un-normalized intensity to compare the absolute differences between the RBE and the quiet background.

From Figs. 2 and 3, we see that the strongest Doppler shifts of the Ca II K line-minimum, those of RP−0, 5, and 8, are associated with the strongest K_2 features at the opposite wavelengths. The line-minimum of RP−3 has the same Doppler shift as RP−0 but approximately the same K_2 intensity when measured relative to its line-minimum. RP−1 and 4 show both the smallest shifts and the weakest K_2 peaks. Together with the completeness of the k-means clustering method and the reduced number of clusters where spicules are present. This establishes a clear relation between the Doppler shift of the line-minimum and the brightness of the K_2 peaks.

Besides intensity, the K_2 features seem to strengthen in width, but the different peaks differ to the greatest extent in the wavelengths towards the line-minimum. Notably, for RBEs, there is no widening of the K_2 in the direction opposite to the new line-minimum, with the associated K_1 and immediate surrounding line-wing slopes being almost identical for all RPs. For RREs the widening is overwhelmingly towards the shifted K_3; thus, the width change of the K_2 features is likely associated with the removal of the K_3 feature from the wavelengths where the widening is observed.

The maxima of the Hα differential profiles (as in Rouppe van der Voort et al. 2009) for RP−3 and 8, plotted in Figs. 2 and 3, nearly match the shifted Ca II K line-minima. Such a match suggests that that particular wavelength position has a physical meaning.

Motivated partially by a similar asymmetric broadening of Ca II K_2, Athay (1970) modeled K_2 grain enhancements using strong flows of opposite direction to that expected by their spectral position and found differential opacity shifts
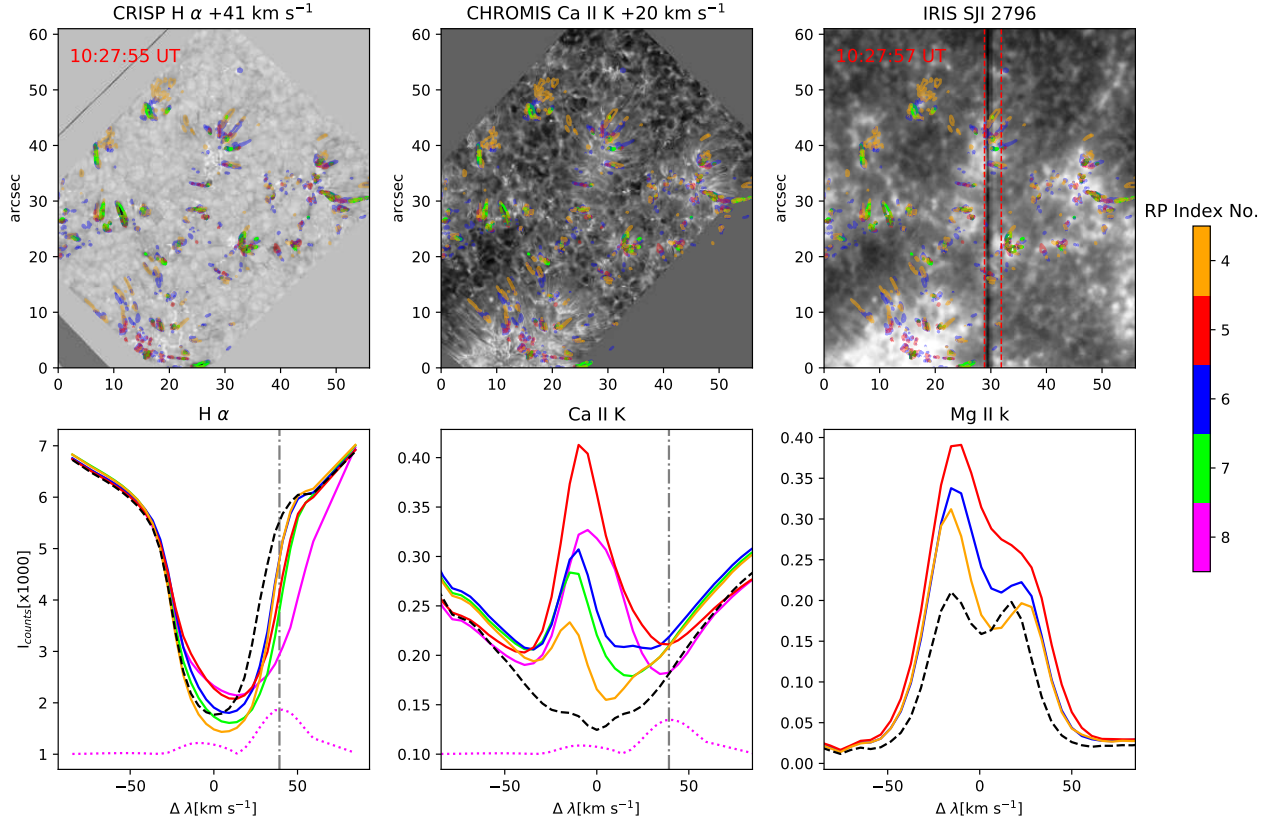
Fig. 3. Rapid red-shifted excursions in Hα, Ca II K and Mg II k in the same format as Fig. 2.

dominating the enhancements, with flow-driven source function changes being small and relatively unimportant. Flow-driven source function enhancements can be important for K_3 formation (Scharmer 1981, 1984) via capture of deeper more intense radiation. With time-dependent forward modeling, Carlsson & Stein (1997) explained the formation of Ca II H and K bright grains, where velocity gradients were important in amplifying shock-driven source function enhancements. Similarly, de la Cruz Rodríguez et al. (2015a) found a non-local thermodynamic equilibrium (NLTE) source function increase of the Ca II 8542 line, enhanced in the red and suppressed in the blue via a differential upflow. In this trend, NLTE Ca II 8542 inversions by Henriques et al. (2017) and Bose et al. (2019) showed that strong differential downflows in the upper atmosphere would best generate the blue-shifted emission features of umbral flashes, with Bose et al. (2019) finding evidence that such downflows could explain observed asymmetries in the Mg II k profiles.

Based on the relations identified in this discussion, we propose that the line formation of the most strongly shifted RBEs (RREs) is dominated by a combination of the Doppler shift of the K_3, completely suppressing one of the K_2 peaks, and an "opacity window" effect, where K_2 features opposite in wavelength to the flow direction are enhanced "in place" due to differential Doppler removal of upper-layer opacity. For the RBE case, the K_2 suppression is such that their intensity is as low as that of the quiet average. Such insensitivity to the lower layers, together with the match with the Hα differential profiles, further indicates that the line-minimum is the Doppler-shifted K_3, and that its position is representative of the true mass velocity of the spicule, and therefore the defining feature to search for in spicule Ca II K studies.

While symmetrical in shape to RBEs and featuring the same relations that lead us to the identification of both the opacity window effect and of a flow-dominated K_3, RRE RPs are different from RBE RPs in intensity levels. For both Mg II k and Ca II K the overall light levels of most RRE RPs depart significantly from the quiet reference case and show elevated line-minimums in Hα, while RBEs do not. This suggests the contribution of other line-forming mechanisms to RREs, possibly related to heating (but then leading to raised Hα profiles rather than mere broadening), in a way beyond the scope of this Letter.

3.2. Where do we "see" the RBEs and RREs in Ca II K?

From the spectroheliograms observed in the Ca II K it is clear that, unlike Hα, identifying spicules based on their contrast with respect to the background is a challenging task. We selected one RBE and one RRE, in Hα and Ca II K, as shown in Fig. 4, with more examples shown in Appendix C. From the former, it is clear that the same spicules that are present in Hα (top row) are also present, with almost the same shape and absorption character, in the line-minimum of Ca II K (second row) which, as visible in the inset profiles, is the Doppler-shifted K_3. In the third row of Fig. 4, where the K_2 wavelengths have been selected to generate an image, the contrast of the RBEs and RREs is visibly much lower than the contrast of the K_3 feature. More strikingly, the patterns such as bright points and bright lanes from the lower layers (bottom row) are distinctly visible in the K_2 image, whereas for the K_3 images no background patterns are ever discernible along the body of the spicule. This is consistent with the suggested line-formation hypothesis put forward, that is, when we observe the K_2 feature of RBEs and RREs (as we do in the
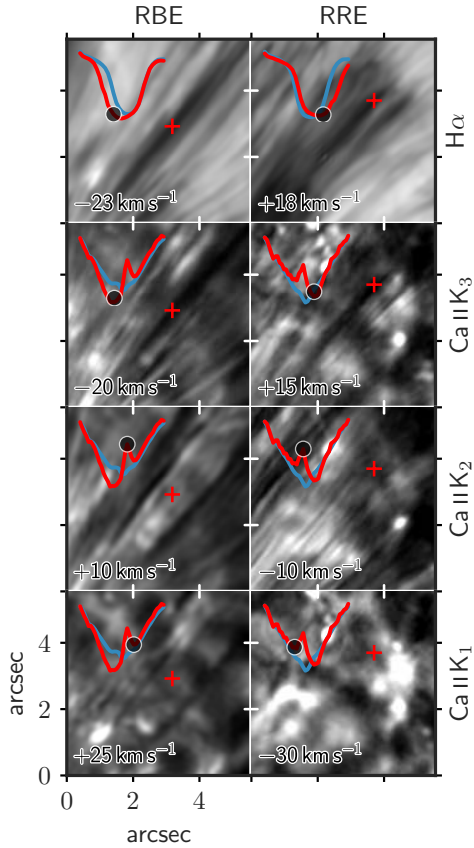
Fig. 4. RBEs and RREs with surroundings in the Hα line wing, and their Ca II K_3, K_2, and K_1 wavelengths. Crosses mark the red inset profile spatial locations and the circles mark the selected wavelengths. The blue profile is the median over the area shown.

third row of Fig. 4), we primarily observe a background-driven enhancement via photons shining through the "window".

3.3. Rapid blue and red-shifted excursions in Mg II k

Figures 2 and 3 include co-temporal and co-spatial SST and IRIS SJIs, as well as IRIS Mg II k spectra that match the color scheme used for Ca II K. The core of the Mg II k spectra are Doppler shifted to the blue (red) in tandem with the shifts in the Ca II K core and at the same time, the opposite k_2 peaks are enhanced, suggesting the same opacity shift and window effects present as in Ca II K. Such effects do not seem as pronounced as for the Ca II K spectra. This may be due to the slenderness of the spicules, leading to mixing of profiles for the lower-resolution IRIS data, further exacerbated by the two-pixel binning. Moreover, Mg II k spectra corresponding to the RPs with the strongest k_3 absorption are absent, as such spicules occurred outside of the IRIS slit sampling. Still, from the at-rest case (black dashed profile) to all RBE and RRE RPs, one sees the expected relationship changes, with a k_3 shift leading to a suppressed k_2 and opposite enhanced k_2, matching their corresponding Ca II K relations. We note that RP−0 k_3 has nearly the same Doppler shift as RP−1, and likewise nearly the same Hα asymmetry. Unsurprisingly, they show a similar k_2 to k_3 relation.

Both the RBE and the RRE Mg II k profiles have a higher intensity compared to the average background. Further, the RP−5 in Fig. 3, the most strongly shifted in Ca II K that is present in Mg II k, shows a complete suppression of k_{2R}. A very similar complete suppression, but for the RBE case, can be seen in

Fig. 1g of Rouppe van der Voort et al. (2015) which, in turn, is at the maximum excursion of the k_3 (λt diagram therein). This literature example fits and supplements the relations between spectral features that we identify for both Ca II K and Mg II k, and is qualitatively reproduced by the following numerical experiment.

3.4. Radiative transfer computations

We performed a simple forward modelling based on radiative transfer computations where all the three spectral profiles, Hα, Ca II K, and Mg II k, were synthesized using the RH1.5D code (Uitenbroek 2001; Pereira & Uitenbroek 2015). We used the standard five-level plus continuum models of hydrogen (H I) and calcium (Ca II) from RH1.5D and a ten-level plus continuum model of Mg II. The profiles were synthesized using the FAL-C atmosphere (Fontenla et al. 1993) with modified LOS velocity stratifications as shown in Fig. 5. These consisted of a gradient in velocity (Fig. 5, rightmost column), at a height where the core of Ca II K is most sensitive, with maximum velocities of ±30, ±25 and ±20 km s^{-1}.

The two rows of Fig. 5 show the synthetic RBE (RRE)-like intensity profiles for three different negative (positive) LOS velocity stratifications. The dashed spectra plot the at-rest case.

In this simple experiment, we see that, as apparent from the observations, the Doppler shifts of the K_3 and k_3 features are the same as the velocities of the upper layers; that they suppress a K_2 and k_2 peak; and that the opposite-in-offset K_2 and k_2 peaks are enhanced without a Doppler-shift and are widened in the direction of the line-core as would be explained by the "window" effect.

The main difference between the Ca II K and the Mg II k cases is that the latter shows a residual peak that could be erroneously interpreted as a flow at that Doppler shift.

4. Conclusions

We find that Ca II K and Mg II k spicule line formation is dominated by opacity shifts and associated opacity "windows". We find indications for other mechanisms, likely heating-based, in the enhancement of the K_{2V} (k_{2V}) peaks for RREs but opacity-shift and "window" relations are always present and dominant.

We find that a basic model, generated only with this understanding and a simple gradient in velocity from at-rest to strong velocities in the upper chromospheric layers, effectively reproduces the main properties of the observed spicule profiles.

The wavelength position of the K_2 (k_2) peaks is not directly usable as a velocity diagnostic for spicules. In practical terms, the Doppler shift of the K_3 (k_3) features provides an accurate velocity measure; one that is consistent across multiple lines. The spicule Doppler shifts that we measure from Ca II K to be in the range 20−50 km s^{-1} confirm earlier spicule Doppler measurements from other spectral lines (Rouppe van der Voort et al. 2009; Kuridze et al. 2016), largely removing concern over statistics based on Hα differential profiles and reservations about the presence of such flows (Judge et al. 2011). These Doppler measurements constitute the LOS component of the mass flow in spicules. Due to our top-down viewing angle, these flows could directly be compared to the apparent spicule velocities of up to 150 km s^{-1} measured nearly perpendicular to the limb (De Pontieu et al. 2007; Pereira et al. 2012, 2014; Skogsrud et al. 2015), had they been actual mass flows. Due to the completeness of our k-mean clustering analysis and the absence of such high Doppler velocities, this Letter presents resolving evidence that >100 km s^{-1} limb apparent motions cannot be attributed to mass flows and must be due
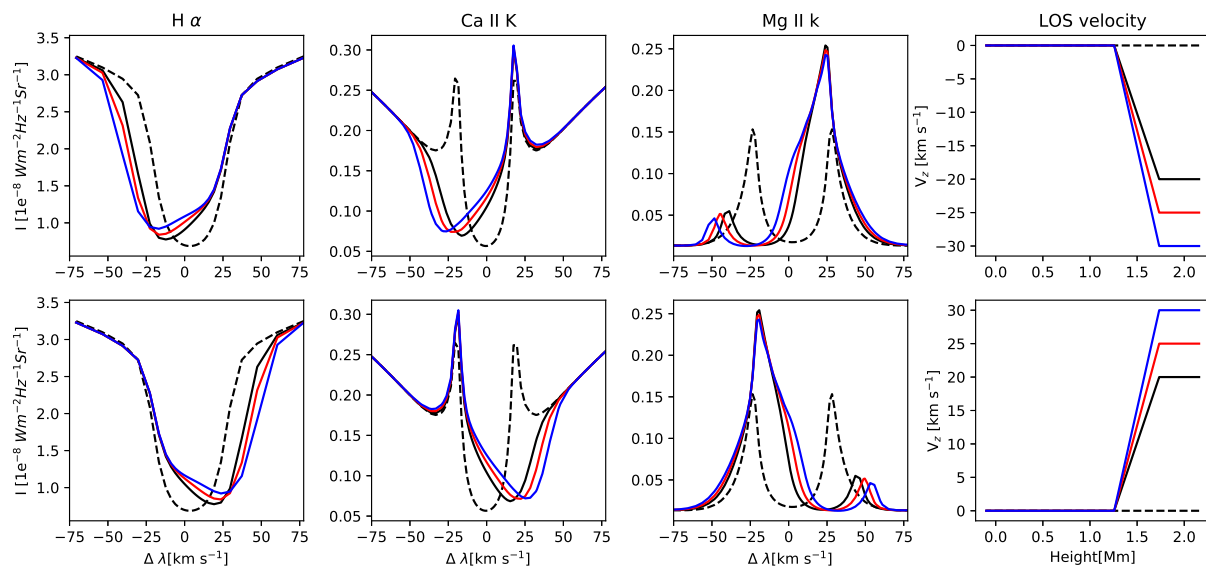
Fig. 5. Forward modeling of Hα, Ca II K, and Mg II k spectra using the RH1.5D code. *Top row*: synthetic RBE-like profiles with a negative line-of-sight (LOS) velocity stratification with a minimum velocity of −30 (blue), −25 (red), and −20 (black) km s^{-1}. *Bottom row*: synthetic RRE-like profiles modeled in the same way as the RBEs except for the positive velocity stratification with a maximum velocity of +30 (blue), +25 (red), and +20 (black) km s^{-1}, respectively. The dashed black lines show the spectra with zero velocity in all the three wavelengths.

to other mechanisms such as rapidly propagating heating fronts (De Pontieu et al. 2017b).

References

Arthur, D., & Vassilvitskii, S. 2007, in Proceedings of the Eighteenth Annual ACM-SIAM Symposium on Discrete Algorithms, Soc. Ind. Appl. Math., 1027
Athay, R. G. 1970, Sol. Phys., 11, 347
Bjørgen, J. P., Sukhorukov, A. V., Leenaarts, J., et al. 2018, A&A, 611, A62
Bose, S., Henriques, V. M. J., Rouppe van der Voort, L., & Pereira, T. M. D. 2019, A&A, 627, A46
Carlsson, M., & Stein, R. F. 1997, ApJ, 481, 500
de la Cruz Rodríguez, J., Hansteen, V., Bellot-Rubio, L., & Ortiz, A. 2015a, ApJ, 810, 145
de la Cruz Rodríguez, J., Löfdahl, M. G., Sütterlin, P., Hillberg, T., & Rouppe van der Voort, L. 2015b, A&A, 573, A40
De Pontieu, B., McIntosh, S., Hansteen, V. H., et al. 2007, PASJ, 59, S655
De Pontieu, B., McIntosh, S. W., Carlsson, M., et al. 2011, Science, 331, 55
De Pontieu, B., Title, A. M., Lemen, J. R., et al. 2014, Sol. Phys., 289, 2733
De Pontieu, B., De Moortel, I., Martinez-Sykora, J., & McIntosh, S. W. 2017a, ApJ, 845, L18
De Pontieu, B., Martínez-Sykora, J., & Chintzoglou, G. 2017b, ApJ, 849, L7
Everitt, B. S. 1972, Br. J. Psychiatry, 120, 143
Fontenla, J. M., Avrett, E. H., & Loeser, R. 1993, ApJ, 406, 319
Henriques, V. M. J. 2012, A&A, 548, A114
Henriques, V. M. J., Kuridze, D., Mathioudakis, M., & Keenan, F. P. 2016, ApJ, 820, 124
Henriques, V. M. J., Mathioudakis, M., Socas-Navarro, H., & de la Cruz Rodríguez, J. 2017, ApJ, 845, 102

Iijima, H., & Yokoyama, T. 2015, ApJ, 812, L30
Judge, P. G., Tritschler, A., & Chye Low, B. 2011, ApJ, 730, L4
Kontogiannis, I., Gontikakis, C., Tsiropoula, G., & Tziotziou, K. 2018, Sol. Phys., 293, 56
Kuridze, D., Henriques, V., Mathioudakis, M., et al. 2015, ApJ, 802, 26
Kuridze, D., Zaqarashvili, T. V., Henriques, V., et al. 2016, ApJ, 830, 133
Langangen, Ø., De Pontieu, B., Carlsson, M., et al. 2008, ApJ, 679, L167
Leenaarts, J., Pereira, T. M. D., Carlsson, M., Uitenbroek, H., & De Pontieu, B. 2013, ApJ, 772, 90
Löfdahl, M. G., Hillberg, T., de la Cruz Rodriguez, J., et al. 2018, ArXiv e-prints [arXiv:1804.03030]
Martínez-Sykora, J., De Pontieu, B., Hansteen, V. H., et al. 2017, Science, 356, 1269
Martínez-Sykora, J., De Pontieu, B., De Moortel, I., Hansteen, V. H., & Carlsson, M. 2018, ApJ, 860, 116
Pereira, T. M. D., & Uitenbroek, H. 2015, A&A, 574, A3
Pereira, T. M. D., De Pontieu, B., & Carlsson, M. 2012, ApJ, 759, 18
Pereira, T. M. D., De Pontieu, B., Carlsson, M., et al. 2014, ApJ, 792, L15
Pereira, T. M. D., Rouppe van der Voort, L., & Carlsson, M. 2016, ApJ, 824, 65
Rouppe van der Voort, L., Leenaarts, J., De Pontieu, B., Carlsson, M., & Vissers, G. 2009, ApJ, 705, 272
Rouppe van der Voort, L., De Pontieu, B., Pereira, T. M. D., Carlsson, M., & Hansteen, V. 2015, ApJ, 799, L3
Rutten, R. J., & Uitenbroek, H. 1991, Sol. Phys., 134, 15
Scharmer, G. B. 1981, ApJ, 249, 720
Scharmer, G. B. 1984, in Accurate Solutions to Non-LTE Problems Using Approximate Lambda Operators, ed. W. Kalkofen, 173
Scharmer, G. B., Bjelksjö, K., Korhonen, T. K., Lindberg, B., & Petterson, B. 2003a, in Innovative Telescopes and Instrumentation for Solar Astrophysics, eds. S. L. Keil, & S. V. Avakyan, SPIE Conf. Ser., 4853, 341
Scharmer, G. B., Dettori, P. M., Löfdahl, M. G., & Shand, M. 2003b, in Society of Photo-Optical Instrumentation Engineers (SPIE) Conference Series, eds. S. L. Keil, & S. V. Avakyan, 4853, 370
Scharmer, G. B., Narayan, G., Hillberg, T., et al. 2008, ApJ, 689, L69
Sekse, D. H., Rouppe van der Voort, L., & De Pontieu, B. 2012, ApJ, 752, 108
Sekse, D. H., Rouppe van der Voort, L., De Pontieu, B., & Scullion, E. 2013, ApJ, 769, 44
Skogsrud, H., Rouppe van der Voort, L., De Pontieu, B., & Pereira, T. M. D. 2015, ApJ, 806, 170
Tian, H. 2017, Res. Astron. Astrophys., 17, 110
Tsiropoula, G., Tziotziou, K., Kontogiannis, I., et al. 2012, Space Sci. Rev., 169, 181
Uitenbroek, H. 2001, ApJ, 557, 389
van Noort, M., Rouppe van der Voort, L., & Löfdahl, M. G. 2005, Sol. Phys., 228, 191
Vissers, G., & Rouppe van der Voort, L. 2012, ApJ, 750, 22

Appendix A: Observations and data processing

The enhanced network region was observed in a coordinated SST and IRIS campaign on 25 May 2017 and was centered on heliocentric solar coordinates $(x, y) = (31'', -89'')$ with corresponding observing angle $\mu = \cos\theta = 0.99$ (θ being the heliocentric angle). The time duration of the observations was about 97 min starting from 09:12 UT until 10:49 UT. We used both the CRISP and CHROMIS tunable Fabry-Pérot instruments to record the data from the SST. CHROMIS was installed in 2016 and will be described in a forthcoming paper by Scharmer and collaborators. CRISP sampled the Hα and Fe I 6302 Å absorption lines in imaging spectroscopic and spectropolarimetric mode respectively at a temporal cadence of 19.6 s and spatial sampling of $0''\!.058$. The Hα spectra were sampled at 32 wavelength positions between ± 1.85 Å with respect to the line core. CHROMIS sampled Ca II K at 41 wavelength positions within ± 1.28 Å with 63.5 mÅ steps. In addition, a continuum position was sampled at 4000 Å. The temporal cadence of the CHROMIS data was 13.6 s with an image scale of $0''\!.038$. The SST diffraction limit λ/D (with $D = 0.97$ m being the effective aperture) is equal to $0''\!.08$ at 3934 Å. High spatial resolution was achieved through excellent seeing conditions, the SST adaptive optics system (an upgrade of the system described in Scharmer et al. 2003b), and the Multi-Object Multi-Frame Blind Deconvolution (MOMFBD, van Noort et al. 2005) image restoration technique. The CRISP pipeline (de la Cruz Rodríguez et al. 2015b) and an early version of the CHROMIS pipeline (Löfdahl et al. 2018) were used for further data reduction, both including the spectral consistency method of Henriques (2012). The CRISP data were aligned to the CHROMIS data through cross-correlation of the photospheric wideband channels, for CRISP with a full-width at half maximum ($FWHM$) = 4.9 Å centered at the Hα line and for CHROMIS with a $FWHM$ = 13.2 Å centered between the Ca II H and K lines at 3950 Å.

The IRIS was running a so-called "medium-dense 8-step raster" program (OBS-ID 3633105426) with 2 s exposure time and continuous $0''\!.34$ steps of the spectrograph slit covering a field-of-view of $2''\!.32$ and $69''\!.2$ in the solar-X and Y directions respectively, spatially and spectrally binned by a factor of two. The cadence of the rasters is 25 s. In addition, IRIS recorded slit-jaw images in the 2796 Å channel (dominated by Mg II k core and inner wings) as well as 1400 Å with exposure times of 2 s, pixel scale of $0''\!.33$ and a FOV of $64''\!.2 \times 69''\!.2$ in the solar X and Y directions.

The IRIS data were aligned to the SST data (blown up to the CHROMIS pixel scale) by cross-correlating the Ca II K inner line-wings with the 2796 SJI. The datasets were initially investigated using CRISPEX (Vissers & Rouppe van der Voort 2012).

Appendix B: k-means clustering

Commonly used in machine-learning applications, the k-means clustering technique (Everitt 1972) is defined as one where a certain number of observations in a data set are partitioned into k clusters, where each observation is represented by a cluster with the closest mean. It is a very simple but robust algorithm that is primarily based on the following steps: (1) choose k measurements as initial clusters centers; (2) compute the Euclidian distances between each observed point x in the data and the cluster centers μ given by $\sum_{i=1}^{n} \sum_{j=1}^{k} \|x^{(i)} - \mu^{(j)}\|$, where $\| \bullet \|$ represents the Euclidian distance; (3) assign an observed point to the closest cluster center by minimizing the sum of squared errors
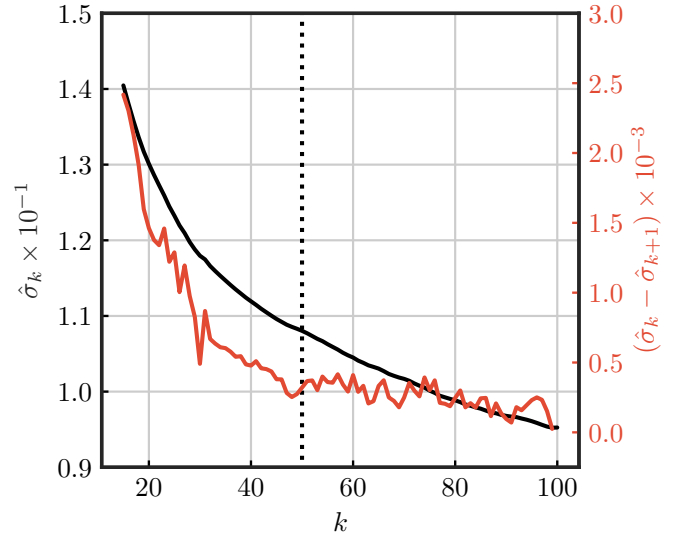
Fig. B.1. Finding the optimum number of clusters, k, for classification of the combined Hα and Ca II K line profiles using the k-means technique. The black curve denotes $\hat{\sigma}_k$, the mean of standard-deviation within the clusters for k clusters, whereas, $\hat{\sigma}_k - \hat{\sigma}_{k+1}$ is presented by the red curve. The estimated optimum number for clusters, $k = 50$, is indicated by the dotted vertical line.

within each cluster; (4) recompute the new cluster centers by averaging all the observations in each cluster; and (5) repeat steps (2)–(4) until none of the observations changes its cluster in two successive iterations, thereby reaching convergence. One of the major limitations is that the result of the clustering (also the number of iterations required) depends significantly on the initialization (step (1)). To circumvent this problem, we used the `k-means`++ (Arthur & Vassilvitskii 2007) method of initialization, where once the first cluster center is drawn randomly, the idea is to chose the newer cluster centers in a way that they are far from the previously chosen ones.

The k-means algorithm was used to cluster the Stokes I profiles by simultaneously combining the co-aligned Hα and Ca II K spectra for each pixel on the FOV, as shown in Fig. 1. The major advantage of applying this technique to the combined spectra was to identify features based on their spectral signatures in Hα and infer the corresponding signature in Ca II K.

Before applying the k-means to the observations, the Hα and Ca II K spectra were normalized by a factor, I_w. For each Hα spectrum, I_w is the intensity of the shortest wavelength observed, whereas I_w for each Ca II K spectrum is also the intensity of the shortest wavelength observed but multiplied by a factor, 0.14. Here, 0.14 is the average intensity of the shortest wavelength observed in the Ca II K line over the entire FOV normalized to the average continuum intensity at 4000 Å. This normalization is important, especially for the Ca II K spectra, to avoid large pixel-to-pixel intensity fluctuations in the line wings caused by photospheric variations, thereby allowing the algorithm to focus on the line profile between K$_{1v}$ and K$_{1r}$ which forms in the chromosphere. The representative profiles shown in Fig. 1 were normalized this way.

It is important to find an optimum number of clusters to use the k-means classification technique more effectively. We used the mean of the standard-deviation within the clusters, $\hat{\sigma}_k$, to find the optimum number of clusters and for this we applied k-means to a subset of our observations (ten scans) with k varying from 15 to 100. Variation of $\hat{\sigma}_k$ with respect to k is shown in Fig. B.1, which indicates that in general $\hat{\sigma}_k$ decreases with higher value of
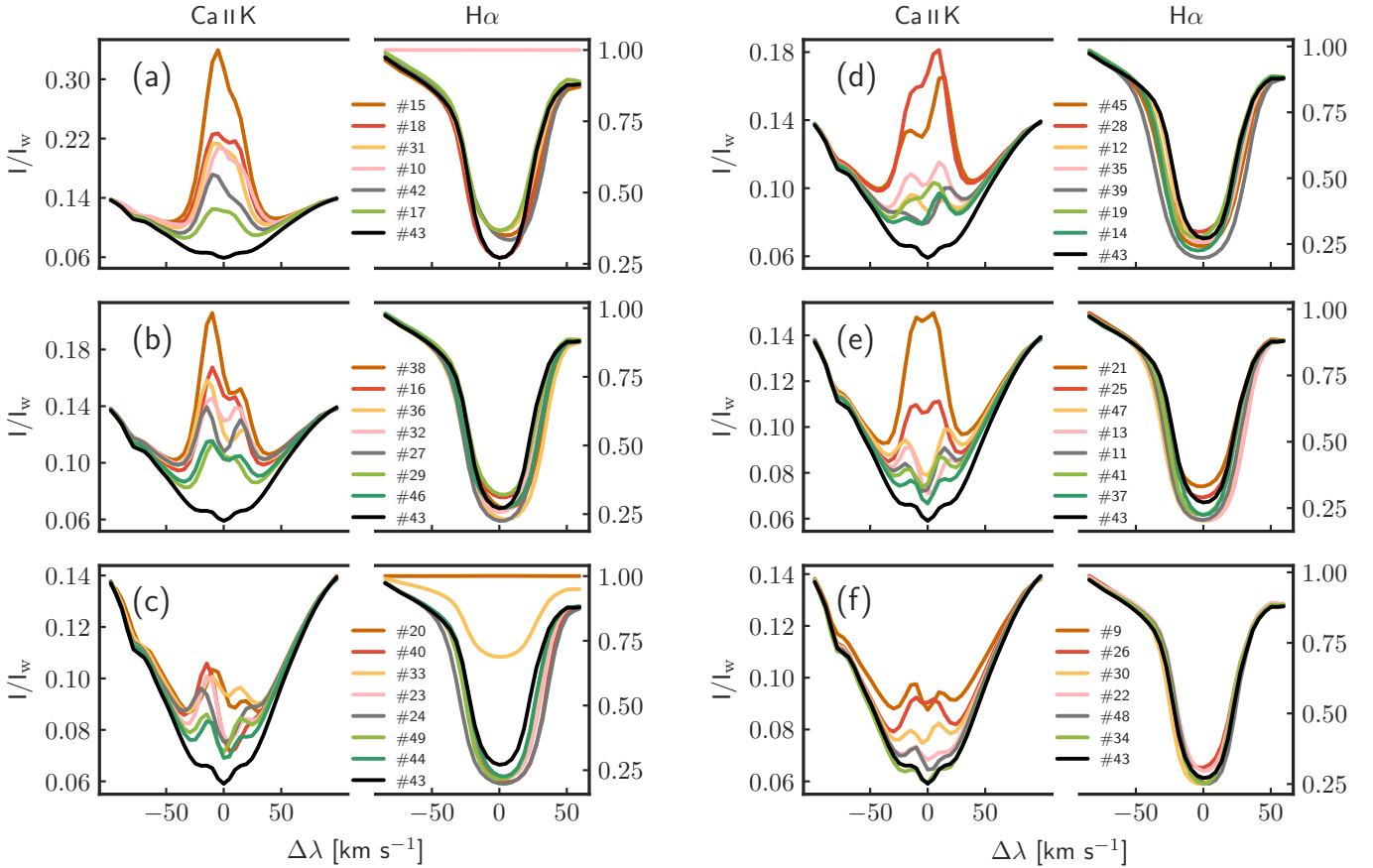
Fig. B.2. Representative profiles obtained by the *k*-means classification of the Hα and Ca II K line profiles. Forty-one RPs (9−49) are presented in six groups in (*panels a–f*). The average quiet-Sun profile represented by RP−43 is shown in all the panels for comparison purposes. Representative profiles 0−3 (RBE profiles) and 4−8 (RRE profiles) are plotted in Figs. 2 and 3, respectively. Here, I_w represents normalizing factor for the intensity, *I*.

k. In principle, $\hat{\sigma}_k$ should reach its minimum when *k* is equal to total number of data points. However it is clear that $\hat{\sigma}_k$ decreases almost linearly after *k* is larger than a certain value, which is ∼50 in our case, and that can be seen by variations in $\hat{\sigma}_k - \hat{\sigma}_{k+1}$ plotted in Fig. B.1. Therefore, based on our analysis of $\hat{\sigma}_k$ we choose *k* = 50 for our *k*-means classification of the Hα and Ca II K line profiles.

We chose ten scans (more than 2×10^7 pixels) at different time steps from the entire time series for training the *k*-means model with 50 initial clusters. This allowed the *k*-means model to assign all the pixels of the training dataset to a particular cluster (as described above). Later, this model was applied to the entire time series that enabled an automatic and unsupervised clustering of the spectra corresponding to all the pixels in the FOV, for each and every time step. One such example is shown in the first row of Fig. 1. Each pixel is assigned to a particular cluster center that is indicated by a representative profile (RP) index. Figure B.2 shows RPs for cluster numbers 9−49, RBE-like RPs (0−3) in the Hα line and corresponding Ca II K RPs are depicted in Fig. 2. Similarly, RRE-like RPs (4−8) are presented in Fig. 3.

We do not include the Mg II k line observed with IRIS in our *k*-means clustering, primarily because it has very limited spatial coverage compared to CRISP and CHROMIS. Instead, we average all the Mg II k profiles spatially and temporally coinciding with a particular cluster obtained with the *k*-means clustering and this way create RPs for the Mg II k line which can be analyzed along with the Hα and Ca II K RPs.

Appendix C: RBEs/RREs in Ca II K spectroheliograms

As discussed in Sect. 3, RBEs (RREs) have Doppler-shifted line minima and spectroheliograms in the corresponding Ca II K_3 wavelength display a spicule morphology that is coherent with that visible in the Hα wing (see Fig. 4). The RBE and RRE K_2 spectroheliogram on the other hand mostly reflects the background area of the spicule. To demonstrate the consistency of the analysis and the interpretation put forward in Sect. 3.2, we present three more examples of RBEs and RREs in Figs. C.1 and C.2, respectively.
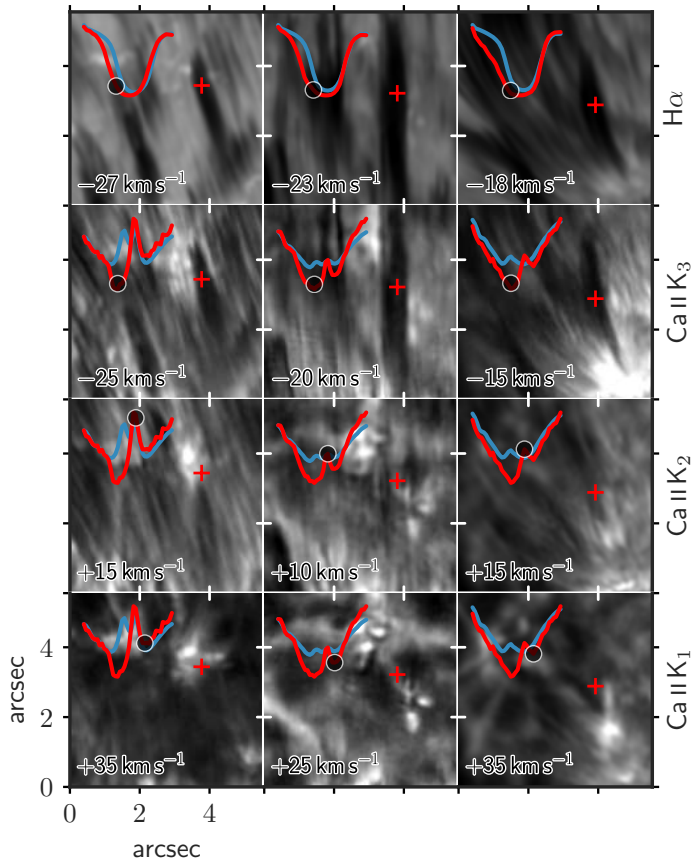
Fig. C.1. Three additional RBE examples in the same format as Fig. 4.
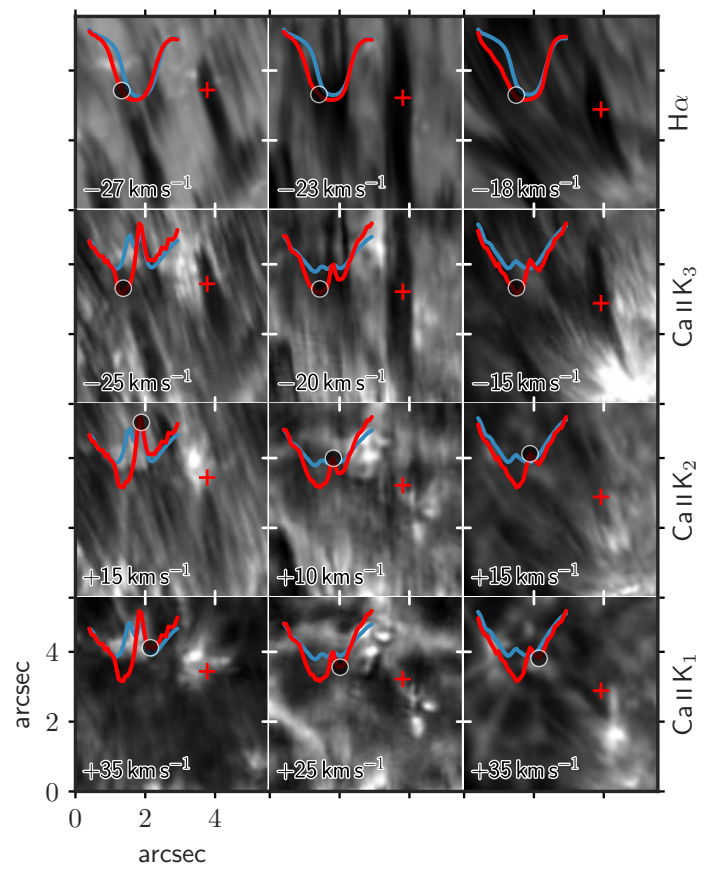
Fig. C.2. Three additional RRE examples in the same format as Fig. 4.